

# Controlled Oxygen Redox for Excellent Power Capability in Layered Sodium-Based Compounds

Hee Jae Kim, Aishuak Konarov, Jae Hyeon Jo, Ji Ung Choi, Kyuwook Ihm, Han-Koo Lee, Jongsoon Kim,\* and Seung-Taek Myung\*

A high-rate of oxygen redox assisted by cobalt in layered sodium-based compounds is achieved. The rationally designed  $\text{Na}_{0.6}[\text{Mg}_{0.2}\text{Mn}_{0.6}\text{Co}_{0.2}]\text{O}_2$  exhibits outstanding electrode performance, delivering a discharge capacity of  $214 \text{ mAh g}^{-1}$  ( $26 \text{ mA g}^{-1}$ ) with capacity retention of 87% after 100 cycles. High rate performance is also achieved at 7C ( $1.82 \text{ A g}^{-1}$ ) with a capacity of  $107 \text{ mAh g}^{-1}$ . Surprisingly, the  $\text{Na}_{0.6}[\text{Mg}_{0.2}\text{Mn}_{0.6}\text{Co}_{0.2}]\text{O}_2$  compound is able to deliver capacity for 1000 cycles at 5C (at  $1.3 \text{ A g}^{-1}$ ), retaining 72% of its initial capacity of  $108 \text{ mAh g}^{-1}$ . X-ray absorption spectroscopy analysis of the O K-edge indicates the oxygen-redox species ( $\text{O}^{2-/1-}$ ) is active during cycling. First-principles calculations show that the addition of Co reduces the bandgap energy from  $\approx 2.65$  to  $\approx 0.61 \text{ eV}$  and that overlapping of the Co 3d and O 2p orbitals facilitates facile electron transfer, enabling the long-term reversibility of the oxygen redox, even at high rates. To the best of the authors' knowledge, this is the first report on high-rate oxygen redox in sodium-based cathode materials, and it is believed that the findings will open a new pathway for the use of oxygen-redox-based materials for sodium-ion batteries.

## 1. Introduction

Recent developments in personal portable devices, electric vehicles, and energy storage systems have mainly been contributed by the evolution of rechargeable lithium-ion batteries (LIBs) to provide more energy density and greater long-term durability. However, because of the ever-increasing demands for these versatile LIBs and the insufficient supply of raw materials such as lithium resources, the price of LIBs is increasing. This concern has led researchers to pay more attention to the exploration of alternatives to LIBs. From this perspective, sodium-ion batteries (SIBs) are attractive because of the abundance of sodium

resources.<sup>[1–5]</sup> However, because of the slightly higher standard electrode potential of sodium ( $-2.7 \text{ V}$  vs the standard hydrogen electrode (SHE)) than lithium ( $-3.02 \text{ V}$  vs SHE), high-capacity electrode materials are needed for SIBs to compensate for their lower operation voltage and to achieve energy densities comparable to those of LIBs. It can be assumed that the cost of SIBs can be lowered relative to that of LIBs because of the cost-effectiveness of sodium resources.<sup>[6]</sup> These factors encourage us to explore potential high-energy-density cathode materials for SIBs.

Among the various crystal structures of Na-containing compounds, layered structures have been intensively investigated because of their high capacity delivered under moderate operation conditions. The related layered structures are classified as O3, P2, P3, etc., according to the stacking sequence of the transition metals and

alkali ions.<sup>[7–9]</sup> Layered sodium transition metal oxides of the form  $\text{Na}_x\text{MO}_2$  ( $\text{M} = \text{Mn, Fe, Co, Ni, Cr, etc.}$ ) are stable in the P2 structure for Na contents ( $x$ ) in the range of 0.3–0.7. This structure enables sodium ion diffusion between the two face-sharing trigonal prismatic sites such that P2-type layered materials generally exhibit higher discharge capacities than other layered materials.<sup>[10–18]</sup>  $\text{Na}_{0.67}\text{MnO}_2$  is one of the most common compounds among P2-type materials.<sup>[19–23]</sup> It delivers a high discharge capacity of over  $175 \text{ mAh g}^{-1}$  but exhibits severe capacity fade during cycling. One of the main reasons for this capacity fade is the structural disintegration caused by the Jahn–Teller effect of  $\text{Mn}^{3+}$  ions in the  $\text{MnO}_6$  octahedra, with elongation of the  $\text{Mn}^{3+}\text{–O}$  distance along one direction. This Jahn–Teller effect can be mitigated by increasing the overall Mn oxidation state by substituting Mn with other elements, such as Ni, Co, Fe, Mg, and Al.<sup>[24–29]</sup> For example, improved cyclability was achieved in Mg-substituted  $\text{Na}_{0.67}\text{Mn}_{1-x}\text{Mg}_x\text{O}_2$  ( $0.0 \leq x \leq 0.2$ ) by suppressing the electrochemical activity of the Jahn–Teller  $\text{Mn}^{3+}$  ions; however, this improvement was attained at the expense of the specific capacity.<sup>[26]</sup>

Recently, Yabuuchi et al.<sup>[27]</sup> introduced a high-capacity P2-type  $\text{Na}_{2/3}[\text{Mg}_{0.28}\text{Mn}_{0.72}]\text{O}_2$  material that exhibited capacities of over  $150 \text{ mAh g}^{-1}$  on charge and  $220 \text{ mAh g}^{-1}$  on discharge by raising the upper voltage cut-off to  $4.6 \text{ V}$ . Note that the average oxidation state of Mn in the compound is  $\approx 3.85+$ , meaning that it cannot exhibit such a high charge capacity. The

H. J. Kim, A. Konarov, J. H. Jo, J. U. Choi, Prof. J. Kim, Prof. S.-T. Myung  
Department of Nano Technology and Advanced Materials Engineering &  
Sejong Battery Institute  
Sejong University  
Gunja-dong, Gwangjin-gu, Seoul 05006, South Korea  
E-mail: jongsoonkim@sejong.ac.kr; smyung@sejong.ac.kr  
Dr. K. Ihm, Dr. H.-K. Lee  
Nano & Interface Research Team  
Pohang Accelerator Laboratory  
Pohang 37673, South Korea

 The ORCID identification number(s) for the author(s) of this article can be found under <https://doi.org/10.1002/aenm.201901181>.

DOI: 10.1002/aenm.201901181

authors suggested that an oxygen-redox process was related to the delivery of such activity in the high-voltage region. Maitra et al.<sup>[30]</sup> experimentally demonstrated the validity of the reversible oxygen redox in the compound. It was observed that alkali-metal ions in the transition-metal layers are indeed not essential for the occurrence of the oxygen-redox reaction, unlike in Li-rich cathode materials.<sup>[31]</sup> These works suggest that the presence of Mg<sup>2+</sup> instead of alkali-metal ions enables the reversible oxygen redox, O<sup>2-/1-</sup>, to be active above 4.2 V. Unfortunately, although the delivered capacity obtained from the transition-metal redox and oxygen redox is one of highest among sodium cathodes, the system suffered from not only serious capacity fading but also poor rate capability because of the sluggish kinetics of the oxygen redox.<sup>[30]</sup> Oxygen-redox reaction is also observed in layered P2-type<sup>[32]</sup> and P3-type<sup>[33]</sup> Na<sub>0.6</sub>[Li<sub>0.2</sub>Mn<sub>0.8</sub>]O<sub>2</sub>, of which Li is used instead of Mg to activate the oxygen redox. The partial substitution of Mn by Li created nonbonding oxygen orbitals due to the Li–O bond being more ionic. This leads to the electrons on Li–O bond to surround on oxygen anion. For P3-type Na<sub>0.5</sub>[Ni<sub>0.25</sub>Mn<sub>0.75</sub>]O<sub>2</sub>, the corresponding redox species are Ni<sup>2+/4+</sup> and O<sup>2-/1-</sup> redox pairs for high voltage operation.<sup>[34]</sup> At fully desodiated state, the formations of Ni<sup>4+</sup> (0.48 Å) and O<sup>1-</sup> (smaller than the ionic radius of O<sup>2-</sup>, 1.4 Å) may contract the crystal structure because of their smaller ionic radii than the starting Ni<sup>2+</sup> (0.69 Å) and O<sup>2-</sup> (1.4 Å). The repeated volume change can cause structural deterioration for long-term cycling, so that minimization of such structural change is preferred to improve the cycling performances. In this point of view, electroinactive Li and Mg are favored to be introduced into the transition-metal layers of layered P2- and P3-type compounds. Moreover, it is thought that electroinactive Mg substitution in Mn sites can result in more stable structure due to the high Pauling's electronegativity of Mg (1.33) relative to Li (0.98).

Given the overlapping in the density of states (DOS) between the oxygen 2p and cobalt 3d (Co<sup>4+/3+</sup>) orbitals in LiCoO<sub>2</sub>,<sup>[35]</sup> which is one of the most representative materials showing good cyclability and acceptable rate performances, we applied this phenomenon to P2-type Na<sub>0.6</sub>[Mg<sub>0.2</sub>Mn<sub>0.8-x</sub>Co<sub>x</sub>]O<sub>2</sub> ( $x = 0.0–0.2$ ), in which the average oxidation state of Mn increases from 3.75+ ( $x = 0.0$ ) to 4+ ( $x = 0.2$ ). Because the oxidation state of Mn is 4+ for Na<sub>0.6</sub>[Mg<sub>0.2</sub>Mn<sub>0.6</sub>Co<sub>0.2</sub>]O<sub>2</sub>, a small capacity induced by Co<sup>3+/4+</sup> was expected. Interestingly, the compound delivered a large capacity of  $\approx 150$  mAh g<sup>-1</sup> on charge. The oxygen K-edge spectra indicate that oxygen is oxidized from O<sup>2-</sup> to O<sup>1-</sup> such that the combination of Co<sup>3+/4+</sup> and O<sup>2-/1-</sup> redox pairs is associated with the electrochemical activity on charge. Note that a high discharge capacity of  $\approx 214$  mAh g<sup>-1</sup> was delivered, which is attributed to the reactions of Co<sup>4+/3+</sup>, O<sup>1-/2-</sup>, and Mn<sup>4+/3+</sup>, and  $\approx 87\%$  (186 mAh g<sup>-1</sup>) of the capacity was retained over 100 cycles. More importantly, the present P2-type Na<sub>0.6</sub>[Mg<sub>0.2</sub>Mn<sub>0.8-x</sub>Co<sub>x</sub>]O<sub>2</sub> was able to deliver discharge capacities of  $\approx 108$  mAh g<sup>-1</sup> for 1000 cycles at a rate of 5C (at 1.3 A g<sup>-1</sup>), showing capacity retention of over 72% (78 mAh g<sup>-1</sup>). This outstanding electrode performance was rationalized by theoretical calculations; namely, the incorporation of Co in the crystal structure was shown to dramatically reduce the bandgap energies. Thus, overlapping of the bandgap energy between oxygen and cobalt is the crucial factor leading to the outstanding electrode performance even at

high rates. Herein, we introduce details of the structural and mechanistic properties of P2-type Na<sub>0.6</sub>[Mg<sub>0.2</sub>Mn<sub>0.8-x</sub>Co<sub>x</sub>]O<sub>2</sub> ( $x = 0.0–0.2$ ) that are activated by the fast oxygen redox.

## 2. Results and Discussion

The crystal structure of the as-synthesized Na<sub>0.6</sub>[Mg<sub>0.2</sub>Mn<sub>0.8-x</sub>Co<sub>x</sub>]O<sub>2</sub> ( $x = 0.0–0.2$ ) compounds were analyzed using Rietveld refinement based on the *P*<sub>6<sub>3</sub>/mmc space group (Figure S1a and Table S1, Supporting Information). The observed and calculated X-ray diffraction (XRD) patterns matched well, and no impurities were detected. Notably, the average oxidation state of Mn increased from 3.75+ to 4+ with increasing Co content in Na<sub>0.6</sub>[Mg<sub>0.2</sub>Mn<sub>0.8-x</sub>Co<sub>x</sub>]O<sub>2</sub> ( $x = 0.0–0.2$ ), as confirmed by the Mn K-edge spectra (Figure S1b, Supporting Information). In addition, a decrease in the lattice parameters was evident with increasing Co content. The incorporated Co<sup>3+</sup> most likely selectively replaced the Mn<sup>3+</sup> in Na<sub>0.6</sub>[Mg<sub>0.2</sub>Mn<sub>0.8-x</sub>Co<sub>x</sub>]O<sub>2</sub> because of their identical valence state, which reflects the increase in the average oxidation state of Mn toward 4+. With consideration of the ionic radii of Co<sup>3+</sup> (0.545 Å), Mn<sup>3+</sup> (0.645 Å), and Mn<sup>4+</sup> (0.53 Å), it is reasonable to consider the replacement of Mn<sup>3+</sup> by Co<sup>3+</sup>. This variation resulted in the reduction of the lattice parameters in Figure S1c in the Supporting Information. The synthesized particles in Figure S2 in the Supporting Information appear to be secondary agglomerates; however, the increase in the Co content did not alter the particle morphologies.</sub>

The electrochemical performance of the Na<sub>0.6</sub>[Mg<sub>0.2</sub>Mn<sub>0.8-x</sub>Co<sub>x</sub>]O<sub>2</sub> ( $x = 0.0–0.2$ ) compounds was tested between 1.5 and 4.6 V with a current of 26 mA g<sup>-1</sup> (0.1C) in Na cells. The cells delivered initial discharge capacities of 125, 130, 207, and 214 mAh g<sup>-1</sup> for  $x = 0.0, 0.05, 0.1,$  and  $0.2$  in Na<sub>0.6</sub>[Mg<sub>0.2</sub>Mn<sub>0.8-x</sub>Co<sub>x</sub>]O<sub>2</sub>, respectively (Figure 1a). Co doping resulted in reduction of the capacity below 4 V, which is attributed to the dilution of the Mn<sup>3+</sup> concentration that can be oxidized to Mn<sup>4+</sup> on charge. In contrast, for Na<sub>0.6</sub>[Mg<sub>0.2</sub>Mn<sub>0.6</sub>Co<sub>0.2</sub>]O<sub>2</sub>, for which the average oxidation state of Mn is 4+, the capacity observed below 4 V likely arose from the contribution of the Co<sup>3+/4+</sup> redox because Mn<sup>4+</sup> cannot be further oxidized. Note that the capacity achieved above 4 V was higher than that of the Co-free electrode. It is evident that Co substitution improved the cycling performance in the Na cells (Figure 1c). The cells retained 36%, 45%, 67%, and 87% of the initial capacity for 100 cycles for the  $x = 0.0, 0.05, 0.1,$  and  $0.2$  electrodes, respectively. Although there were large peaks observed at 4.2 V during the first charge for all the samples, the peak became lower in the following cycles but reversible after the first cycle in differentiated curves (Figure S3, Supporting Information). This indicates reversible sodium storage capability. We further investigated the electrode stability for Na<sub>0.6</sub>[Mg<sub>0.2</sub>Mn<sub>0.8-x</sub>Co<sub>x</sub>]O<sub>2</sub> ( $x = 0$  and  $0.2$ ) using electrochemical impedance spectroscopy (EIS) (Figure S4, Supporting Information). For both the fresh cells, the resulting resistance somehow decreased by the incorporation of Co into Na<sub>0.6</sub>[Mg<sub>0.2</sub>Mn<sub>0.8-x</sub>Co<sub>x</sub>]O<sub>2</sub>. During cycling, it is evident that the related charge transfer resistance increased for both electrodes, while the increase in the resistance was mitigated for the Na<sub>0.6</sub>[Mg<sub>0.2</sub>Mn<sub>0.6</sub>Co<sub>0.2</sub>]O<sub>2</sub> compared to the resistance for the

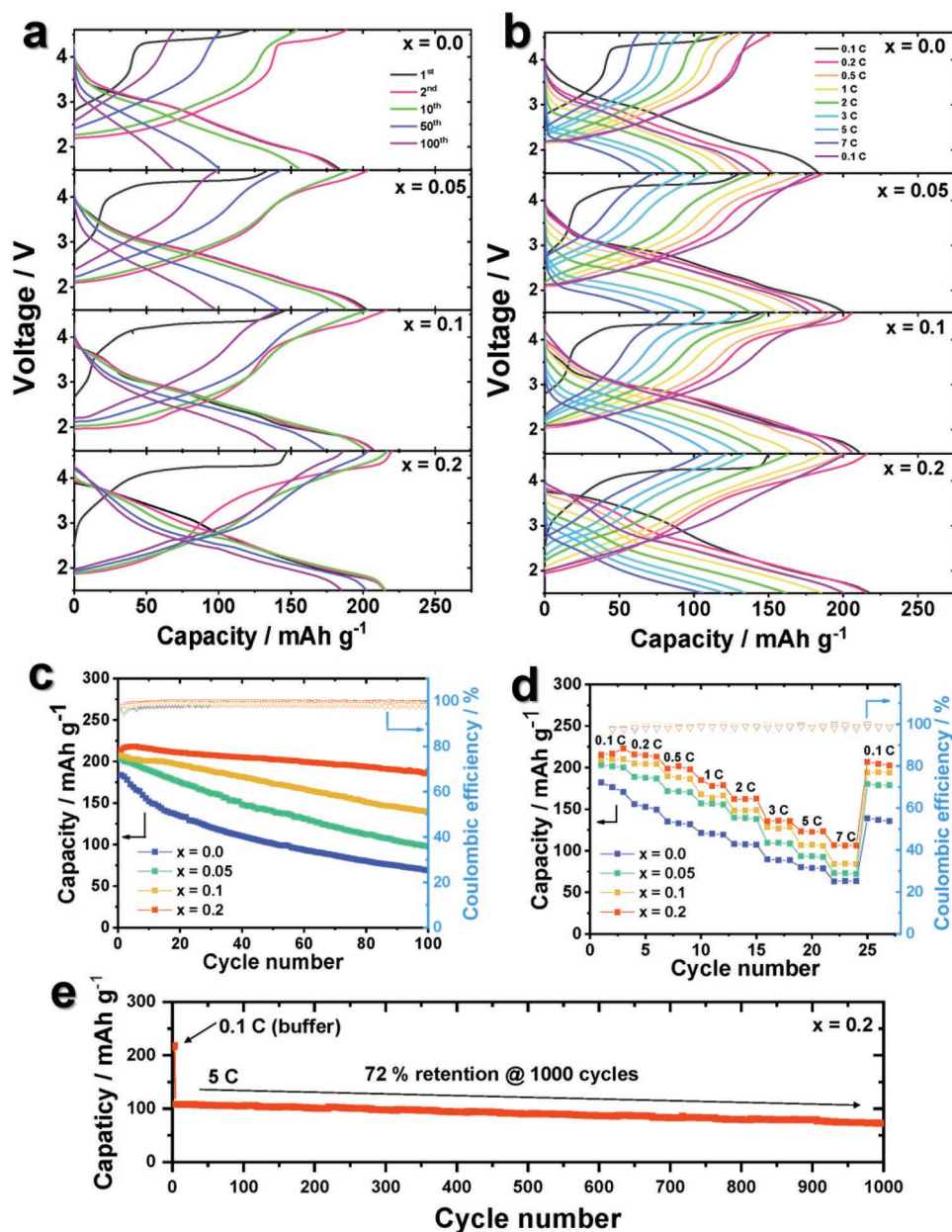


**Figure 1.** a) Voltage profiles of  $\text{Na}_{0.6}[\text{Mg}_{0.2}\text{Mn}_{0.8-x}\text{Co}_x]\text{O}_2$  ( $x = 0.0-0.2$ ) compounds. b) Voltage profiles of  $\text{Na}_{0.6}[\text{Mg}_{0.2}\text{Mn}_{0.8-x}\text{Co}_x]\text{O}_2$  ( $x = 0.0-0.2$ ) at different C-rates. c) Cycling performance of  $\text{Na}_{0.6}[\text{Mg}_{0.2}\text{Mn}_{0.8-x}\text{Co}_x]\text{O}_2$  ( $x = 0.0-0.2$ ) at 0.1C. d) Rate performance of  $\text{Na}_{0.6}[\text{Mg}_{0.2}\text{Mn}_{0.8-x}\text{Co}_x]\text{O}_2$  ( $x = 0.0-0.2$ ). e) Long-term cyclability at 5C for  $x = 0.2$  in  $\text{Na}_{0.6}[\text{Mg}_{0.2}\text{Mn}_{0.8-x}\text{Co}_x]\text{O}_2$ .

Co-free  $\text{Na}_{0.6}[\text{Mg}_{0.2}\text{Mn}_{0.8}]\text{O}_2$ . We also compared the effect of Mg concentration in  $\text{Na}_{0.6}[\text{Mg}_x\text{Mn}_{0.8-x}\text{Co}_{0.2}]\text{O}_2$  ( $x = 0, 0.1, \text{ and } 0.2$ ) crystallized into layered P2 structure in which the average oxidation states of Mn are 3.5+, 3.71+, and 4+, respectively (Figure S5, Supporting Information) and the corresponding electrochemical performance of  $\text{Na}_{0.6}[\text{Mg}_x\text{Mn}_{0.8-x}\text{Co}_{0.2}]\text{O}_2$  ( $x = 0, 0.1, \text{ and } 0.2$ ) in Figure S6 in the Supporting Information. Despite slightly higher capacity of the  $\text{Na}_{0.6}[\text{Mg}_{0.1}\text{Mn}_{0.7}\text{Co}_{0.2}]\text{O}_2$  than that of the Mg-free  $\text{Na}_{0.6}[\text{Mn}_{0.8}\text{Co}_{0.2}]\text{O}_2$ , the resulting capacity was still smaller than that of  $\text{Na}_{0.6}[\text{Mg}_{0.2}\text{Mn}_{0.6}\text{Co}_{0.2}]\text{O}_2$  (Figure 1a; Figure S6, Supporting Information). However, the observed voltage profiles above 4 V were similar to those

of  $\text{Na}_{0.6}[\text{Mg}_{0.2}\text{Mn}_{0.6}\text{Co}_{0.2}]\text{O}_2$ , implying occurrence of similar reaction on high-voltage region. For the reason, we, hereafter, are going to mention on the detailed electrochemical properties and related mechanism for  $\text{Na}_{0.6}[\text{Mg}_{0.2}\text{Mn}_{0.6}\text{Co}_{0.2}]\text{O}_2$ . In addition to the enhanced electrode performance, Co substitution led to excellent rate performance (Figure 1b,d). Even at 7C, the  $\text{Na}_{0.6}[\text{Mg}_{0.2}\text{Mn}_{0.6}\text{Co}_{0.2}]\text{O}_2$  electrode delivered a capacity of 107  $\text{mAh g}^{-1}$ , which is 50% of its capacity at 0.1C (214  $\text{mAh g}^{-1}$ ), and the electrodes for  $x = 0.05$  and  $x = 0.1$  in  $\text{Na}_{0.6}[\text{Mg}_{0.2}\text{Mn}_{0.8-x}\text{Co}_x]\text{O}_2$  delivered 40% of their initial capacity. Moreover, the Co-free electrode,  $\text{Na}_{0.6}[\text{Mg}_{0.2}\text{Mn}_{0.8}]\text{O}_2$ , exhibited only  $\approx 30\%$  of its initial capacity at 7C. In addition, the

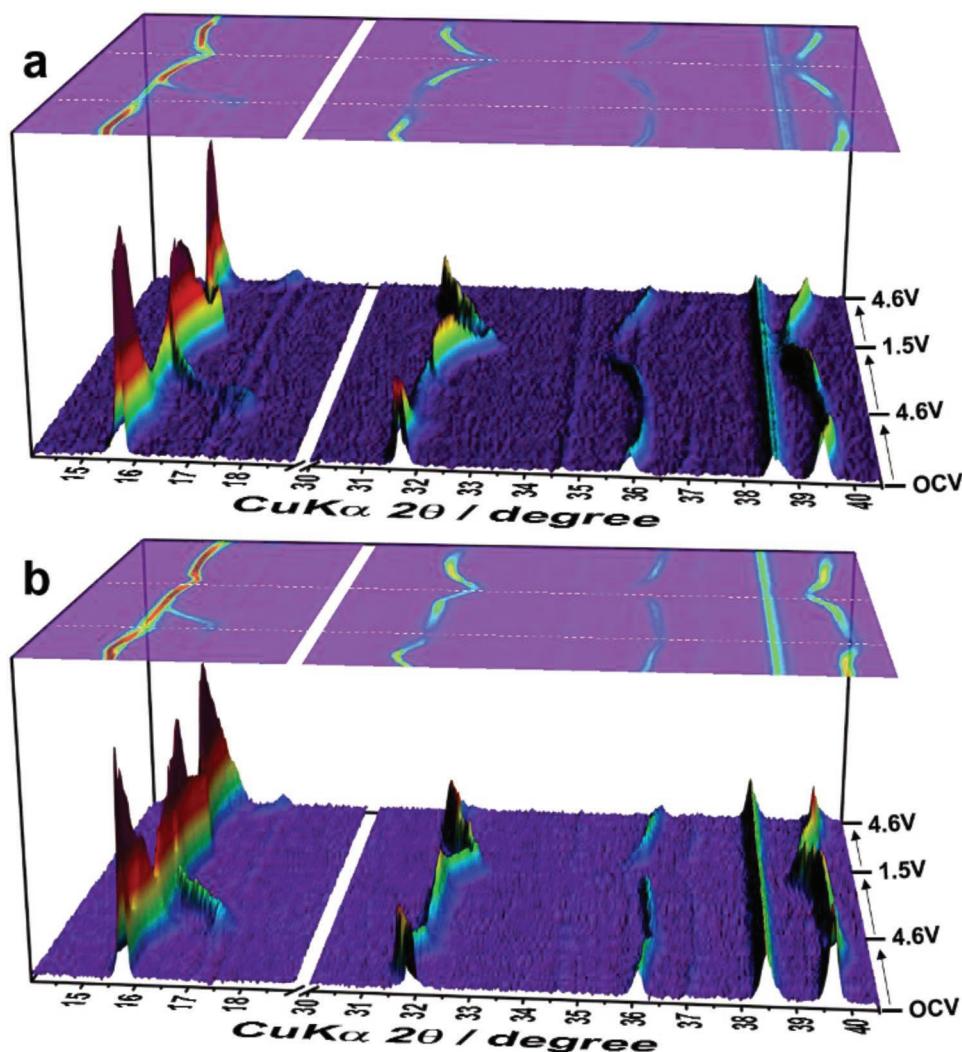


**Figure 2.** Operando XRD patterns of a)  $\text{Na}_{0.6}[\text{Mg}_{0.2}\text{Mn}_{0.8}]\text{O}_2$  and b)  $\text{Na}_{0.6}[\text{Mg}_{0.2}\text{Mn}_{0.6}\text{Co}_{0.2}]\text{O}_2$  electrodes. The measurements were performed during the first charge–first discharge–second charge by applying a current of  $26 \text{ mA g}^{-1}$ .

$\text{Na}_{0.6}[\text{Mg}_{0.2}\text{Mn}_{0.6}\text{Co}_{0.2}]\text{O}_2$  electrode exhibited superior long-term cycling stability at 5C ( $1.3 \text{ A g}^{-1}$ ), with capacity retention of over 72% for 1000 cycles (Figure 1e; Figure S7, Supporting Information).

The operando XRD patterns and corresponding voltage profiles are presented for  $\text{Na}_{0.6}[\text{Mg}_{0.2}\text{Mn}_{0.8}]\text{O}_2$  (Figure 2a; Figure S8a, Supporting Information) and  $\text{Na}_{0.6}[\text{Mg}_{0.2}\text{Mn}_{0.6}\text{Co}_{0.2}]\text{O}_2$  (Figure 2b; Figure S8b, Supporting Information) to explain the structural evolution during the initial cycles. On charge, the P2 phase transformed into the OP4 phase, as confirmed by the peak appearing at  $2\theta = 17.6^\circ$  for both electrodes. This peak returned to its original position after further discharge, and the peak appeared again at the second charge, indicating the occurrence of reversible phase transitions from P2 to OP4 on charge and from OP4 to P2 on discharge. We further examined the XRD patterns at several points on charge and discharge to explore the phase transformation for the  $\text{Na}_{0.6}[\text{Mg}_{0.2}\text{Mn}_{0.6}\text{Co}_{0.2}]\text{O}_2$  electrode at the 100th cycle (Figure S9, Supporting Information). The observed phase transition was consistent with the operando XRD patterns, indicating the occurrence of a

reversible phase transition from the P2 to OP4 phase on charge and vice versa on discharge. These results confirm the structural stability of  $\text{Na}_{0.6}[\text{Mg}_{0.2}\text{Mn}_{0.6}\text{Co}_{0.2}]\text{O}_2$  upon cycling. The calculated lattice parameters from the operando XRD results are presented in Figure S8c,d in the Supporting Information. The  $a$ -axis lattice parameters varied monotonously for both  $x = 0.0$  and  $x = 0.2$  in  $\text{Na}_{0.6}[\text{Mg}_{0.2}\text{Mn}_{0.8-x}\text{Co}_x]\text{O}_2$ . The decrease of the  $a$ -axis lattice parameters is indicative of the oxidation of transition metals such as Mn and Co toward the tetravalent state,  $4+$ , on charging to 4.6 V, which is related to the formation of smaller ionic radii of these metal elements. It is common for the  $c$ -axis lattice parameter of P2-layered sodium transition metal oxides to increase as sodium ions are extracted from the structure because this increase induces a repulsive force between oxygen and oxygen. However, one peculiar point was observed in the refined  $c$ -axis lattice parameter for both  $x = 0.0$  and  $x = 0.2$  in  $\text{Na}_{0.6}[\text{Mg}_{0.2}\text{Mn}_{0.8-x}\text{Co}_x]\text{O}_2$ . The  $c$ -axis parameter decreased after the threshold point, as marked by the red arrow, which corresponds to the voltage plateau on charging. This decrease results from the new alignment of oxygen close packing to form the

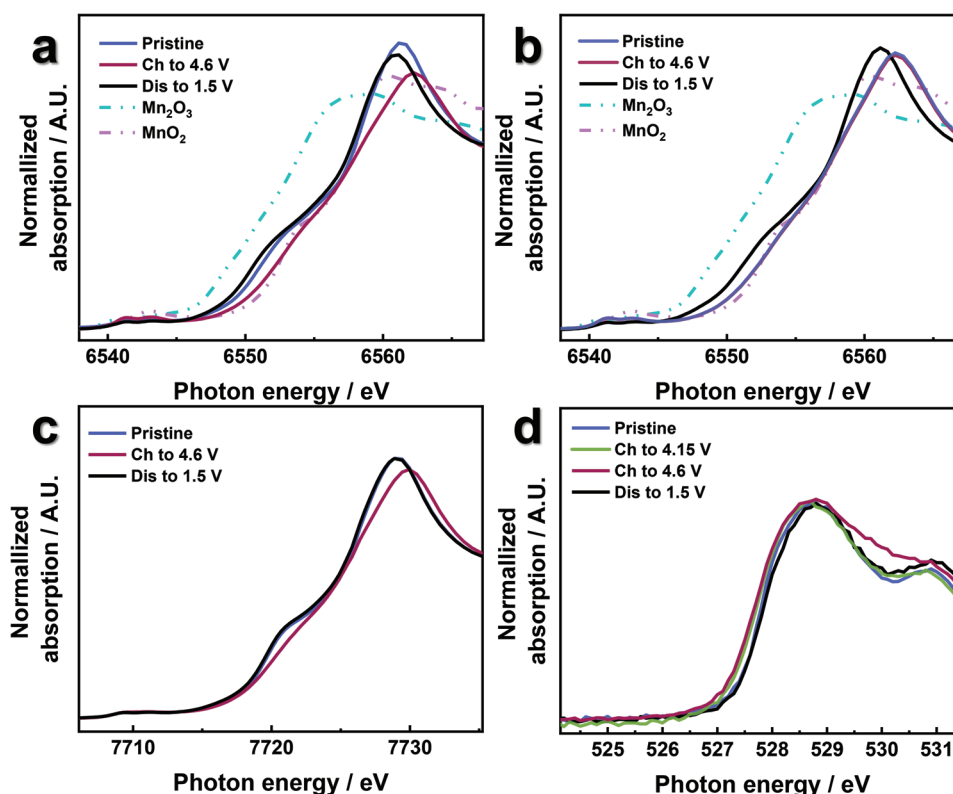


**Figure 3.** Ex situ XANES spectra: a) Mn K-edge spectra of  $\text{Na}_{0.6}[\text{Mg}_{0.2}\text{Mn}_{0.8}]\text{O}_2$ ; b) Mn K-edge spectra and c) Co K-edge spectra of  $\text{Na}_{0.6}[\text{Mg}_{0.2}\text{Mn}_{0.6}\text{Co}_{0.2}]\text{O}_2$ . d) Ex situ XANES O K-edge spectra of  $\text{Na}_{0.6}[\text{Mg}_{0.2}\text{Mn}_{0.6}\text{Co}_{0.2}]\text{O}_2$ .

OP4 phase, as proposed by Lu and Dahn.<sup>[36]</sup> As a result, the  $c$ -axis parameters began to decrease from the threshold point to the end of charge. The appearance of the OP4 phase induced an abrupt change in the  $c$ -axis for these desodiated compounds, specifically, a volume change of  $\approx 11.8\%$  and  $\approx 8.7\%$  for  $x = 0.0$  and  $x = 0.2$  in  $\text{Na}_{0.6}[\text{Mg}_{0.2}\text{Mn}_{0.8-x}\text{Co}_x]\text{O}_2$ , respectively. Notably, although more capacity was observed for  $\text{Na}_{0.6}[\text{Mg}_{0.2}\text{Mn}_{0.6}\text{Co}_{0.2}]\text{O}_2$ , the resulting structure appeared less variable compared with that of the Co-free  $\text{Na}_{0.6}[\text{Mg}_{0.2}\text{Mn}_{0.8}]\text{O}_2$ . On discharge, the reversible tendencies were observed for both compounds.

**Figure 3** presents X-ray absorption near edge structure (XANES) spectra for the Mn, Co, and O K-edges for  $x = 0.0$  and  $x = 0.2$  in  $\text{Na}_{0.6}[\text{Mg}_{0.2}\text{Mn}_{0.8-x}\text{Co}_x]\text{O}_2$  during electrochemical reaction in Na cells. For  $\text{Na}_{0.6}[\text{Mg}_{0.2}\text{Mn}_{0.8}]\text{O}_2$ , the spectrum slightly shifted toward higher energy because of the oxidation of manganese from  $3.75+$  to  $4+$  (Figure 3a). The spectrum shifted to lower energy, even lower than that of the fresh electrode, on discharge to 1.5 V; however, it remained higher than that of  $\text{Mn}^{3+}$ . For  $\text{Na}_{0.6}[\text{Mg}_{0.2}\text{Mn}_{0.8}]\text{O}_2$ , the charge capacity of  $120 \text{ mAh g}^{-1}$  corresponds to the extraction of 0.44 mol of sodium ions,  $\text{Na}_{0.16}[\text{Mg}_{0.2}\text{Mn}_{0.8}]\text{O}_2$ , which results in an average oxidation state of Mn of  $4.225+$ . However, an oxidation state of Mn beyond  $4+$  is not valid in this tested range. The capacity obtained below 4 V is evidently associated with the oxidation of  $\text{Mn}^{3.75+}$  to  $\text{Mn}^{4+}$ , validating the extraction of 0.2 mol of sodium ions, corresponding to  $\approx 57 \text{ mAh g}^{-1}$ . The capacity delivered above 4 V cannot be explained by the oxidation of Mn because the oxidation state of Mn is already  $4+$ ; however, it may be

possible to consider the additional capacity as being contributed by the oxidation of oxygen ( $\text{O}^{2-/-}$ ) from the oxide lattice because of its reversibility rather than the decomposition of the electrolyte, which is irreversible. Although  $\text{Mn}^{4+}$  cannot be further oxidized above  $4+$  within the normal operation window (1.5–5 V vs  $\text{Na}^+/\text{Na}$ ), the removed sodium ion content is  $\approx 0.24 \text{ mol}$  to give  $\text{Na}_{0.16}[\text{Mg}_{0.2}\text{Mn}_{0.8}]\text{O}_2$  when charged to 4.6 V. During discharge, 0.65 mol of sodium ions was intercalated back into the structure, resulting in a capacity of  $183 \text{ mAh g}^{-1}$  assisted by the reversible reduction of the  $\text{O}^{1-}/\text{O}^{2-}$  redox (0.24 mol) followed by reduction of  $\text{Mn}^{4+/3+}$  (0.41 mol) to 1.5 V. This process results in an oxidation state of Mn of  $3.5+$ ,  $\text{Na}_{0.81}[\text{Mg}_{0.2}\text{Mn}_{0.8}^{3.5+}]\text{O}_2$ , which is consistent with the average oxidation state of Mn observed in the Mn K-edge spectra (Figure 3a). For  $\text{Na}_{0.6}[\text{Mg}_{0.2}\text{Mn}_{0.6}\text{Co}_{0.2}]\text{O}_2$ , it is interesting to see that there were no changes in the Mn K-edge spectra on charge (Figure 3b) because the oxidation state of Mn is  $4+$  in the fresh state ( $\text{Na}_{0.6}[\text{Mg}_{0.2}\text{Mn}_{0.6}\text{Co}_{0.2}^{3+}]\text{O}_2$ ). Oxidation of Co from  $\text{Co}^{3+}$  to  $\text{Co}^{4+}$  was observed in the Co K-edge of the XANES spectra on charge (Figure 3c). This result indicates that the initial charge capacity of  $150 \text{ mAh g}^{-1}$  is contributed by the  $\text{Co}^{3+/4+}$  reaction below 4 V and the additional moiety by  $\text{O}^{2-/-}$  redox above 4 V and not the Mn redox because  $\text{Mn}^{4+}$  cannot be further oxidized to 4.6 V ( $\text{Mn}^{4.325+}$  based on the charge capacity). Below 4 V, 0.2 mol of sodium ions are removed by the  $\text{Co}^{3+/4+}$  redox, delivering  $\approx 56 \text{ mAh g}^{-1}$  of the capacity, and the rest of the capacity ( $94 \text{ mAh g}^{-1}$ ) above 4 V is generated by the  $\text{O}^{2-/-}$  redox by extracting 0.334 mol of sodium

ions. During discharge, 0.534 mol of sodium ions are inserted back into the structure by  $\text{Co}^{4+/3+}$  and  $\text{O}^{1-/2-}$  redox pairs; then, the rest of the capacity is contributed by the reduction of Mn from 4+ to 3.62+, which equals 0.228 mol of sodium ions. Overall, 0.726 mol of sodium ions are intercalated back into the structure, resulting in the discharge capacity of  $214 \text{ mAh g}^{-1}$  ( $\text{Na}_{0.828}[\text{Mg}_{0.2}\text{Mn}_{3.62+0.6}\text{Co}_{3+0.2}]\text{O}_{2-2}$ ). Figure 3d presents the O K-edge XANES spectra of  $\text{Na}_{0.6}[\text{Mg}_{0.2}\text{Mn}_{0.6}\text{Co}_{0.2}]\text{O}_2$  charged to 4.15 and 4.6 V and discharged to 1.5 V. When charged to 4.6 V, a new spectral weight appeared at 530 eV for both  $x = 0.0$  and  $x = 0.2$ , which is associated with an increase in the number of oxygen 2p holes, providing evidence of the oxygen-redox reaction occurring at the voltage plateau. Similar phenomena was observed in our previous report.<sup>[37]</sup> This is due to the additional charge transfer of high-valence transition metal clusters, which is consistent with the results of Maitra et al.<sup>[30]</sup> The spectrum returned to its initial state when the electrode was discharged to 1.5 V, indicating the occurrence of a reversible oxygen-redox reaction. X-ray photoelectron spectroscopy (XPS) investigation further evidences the activity of oxygen for  $\text{Na}_{0.6}[\text{Mg}_{0.2}\text{Mn}_{0.6}\text{Co}_{0.2}]\text{O}_2$  in Na cells (Figure S10, Supporting Information). For the fresh electrode, the observed two peaks at 529.6 and 531.4 eV are associated with  $\text{O}^{2-}$  from the crystal structure of  $\text{Na}_{0.6}[\text{Mg}_{0.2}\text{Mn}_{0.6}\text{Co}_{0.2}]\text{O}_2$  and the surface deposited species such as  $\text{Na}_2\text{CO}_3$ , respectively. Note that, in case of the charged electrode, the new peak appeared at 530.1 eV, which is assigned as superoxygen ( $\text{O}^{1-2}$ ) resulted from the oxidation of oxygen bonded with Mn, Mg, and Co elements in the charged  $\text{Na}_{0.6}[\text{Mg}_{0.2}\text{Mn}_{0.6}\text{Co}_{0.2}]\text{O}_2$ . This confirms that capacity is generated by both transition metals and oxygen in the compound. The reversibility of the oxygen redox can be seen from the results of the discharged electrode; namely, the spectrum showed that the new peak at 530.1 eV disappeared but the relative intensity of Me–O (Me: Mn, Mg, and Co) binding increased again at 529.6 eV. The above results indicate that the oxygen redox is involved in delivering capacity and reversible.

The concept of the oxygen-redox reaction controlled by Co substitution was supported by first-principles calculations. We prepared simplified structural models of  $\text{Na}_{0.5}(\text{Mg}^{2+})_{0.25}[(\text{Mn}_{0.75-x}\text{Co}_x)]^{4+}_{0.75}\text{O}_2$  to investigate the oxygen redox activity in  $\text{Na}_{0.6}(\text{Mg}^{2+})_{0.2}[(\text{Mn}_{1-x}\text{Co}_x)]^{4+}_{0.8}\text{O}_2$ . For systematic analysis of the effect of Co substitution on the oxygen-redox reaction, we calculated the density of state of  $\text{Na}_{0.5}(\text{Mg}^{2+})_{0.25}[(\text{Mn}_{0.75-x}\text{Co}_x)]^{4+}_{0.75}\text{O}_2$  for various Co contents ( $x = 0.0, 0.125, 0.25$ ) using the HSE06 hybrid functional and density functional theory (DFT) to provide an appropriate prediction of the oxygen-redox reaction.<sup>[38]</sup> Figure 4 presents the projected DOS (pDOS) of O 2p and Mn 3d for the  $\text{Na}_{0.5}[\text{Mg}_{0.25}\text{Mn}_{0.75}]\text{O}_2$  structure. The electron-occupied state near the Fermi level ( $E_F$ ) was predicted to be affected by the pDOS of O 2p rather than that of Mn 3d, indicating that the Mg substitution enables the  $\text{O}^{2-}/\text{O}^{1-}$  oxygen-redox reaction of  $\text{Na}_x\text{MnO}_2$ . Moreover, Co- and Mg-substituted  $\text{Na}_{0.5}[\text{Mg}_{0.25}\text{Mn}_{0.625}\text{Co}_{0.125}]\text{O}_2$  and  $\text{Na}_{0.5}[\text{Mg}_{0.25}\text{Mn}_{0.5}\text{Co}_{0.25}]\text{O}_2$  also exhibited larger pDOS of O 2p compared with those of not only Mn 3d but also Co 3d in the electron-occupied state near  $E_F$ . These results indicate that the oxygen-redox reaction of  $\text{Na}_{0.5}[\text{Mg}_{0.25}\text{Mn}_{0.625}\text{Co}_{0.125}]\text{O}_2$  and  $\text{Na}_{0.5}[\text{Mg}_{0.25}\text{Mn}_{0.5}\text{Co}_{0.25}]\text{O}_2$  can occur during the charging/discharging process. Co substitution of Mn

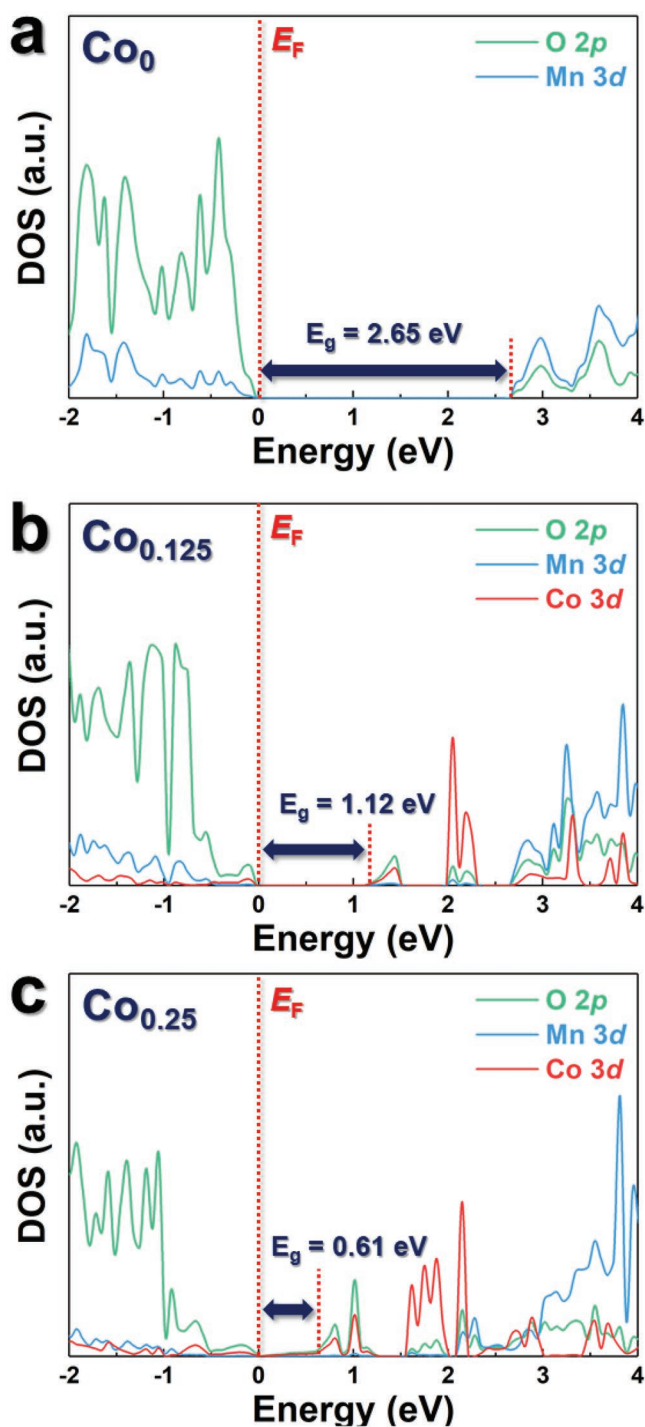


**Figure 4.** pDOS of O 2p, Mn 3d, and Co 3d orbitals for a)  $\text{Na}_{0.5}[\text{Mg}_{0.25}\text{Mn}_{0.75}]\text{O}_2$ , b)  $\text{Na}_{0.5}[\text{Mg}_{0.25}\text{Mn}_{0.625}\text{Co}_{0.125}]\text{O}_2$ , and c)  $\text{Na}_{0.5}[\text{Mg}_{0.25}\text{Mn}_{0.5}\text{Co}_{0.25}]\text{O}_2$ .

sites was also predicted to result in a decrease of the bandgap of  $\text{Na}_{0.5}[\text{Mg}_{0.25}\text{Mn}_{0.75}]\text{O}_2$ , as determined by the relationship between Mn 3d and O 2p; furthermore, its bandgap decreased from  $\approx 2.65$  to  $\approx 0.61$  eV depending on the increase in the substituted Co content in the structure. These first-principles calculation results imply the enhanced electrical conductivity and power capability of Co-substituted  $\text{Na}_{0.5}[\text{Mg}_{0.25}\text{Mn}_{0.5}\text{Co}_{0.25}]\text{O}_2$

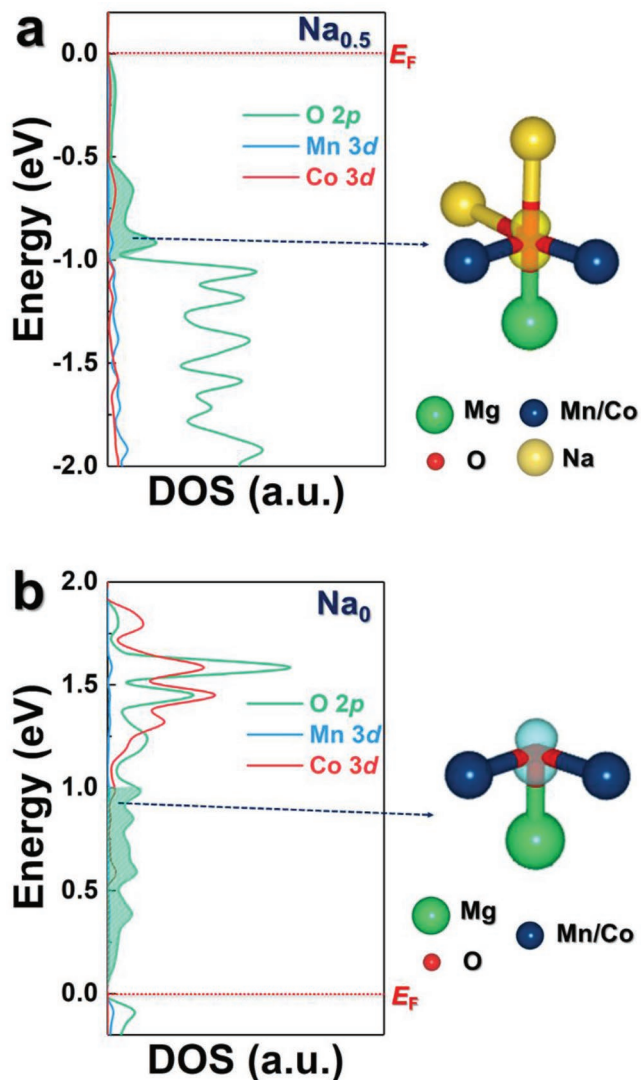


**Figure 5.** pDOS of O 2p, Mn 3d, and Co 3d orbitals for a)  $\text{Na}_{0.5}[\text{Mg}_{0.25}\text{Mn}_{0.5}\text{Co}_{0.25}]\text{O}_2$  and b)  $\text{Na}_0[\text{Mg}_{0.25}\text{Mn}_{0.5}\text{Co}_{0.25}]\text{O}_2$  with the charge density (yellow) and hole density (blue) around the oxygen coordinated by Mg–O–Na coordination.

compared with those of  $\text{Na}_{0.5}[\text{Mg}_{0.25}\text{Mn}_{0.75}]\text{O}_2$ , which agrees well with the findings of earlier work on the superior electrode performance of  $\text{LiCoO}_2$  attributed to the overlapping in the DOS between O 2p and Co 3d ( $\text{Co}^{4+/3+}$ ) orbitals.<sup>[39,40]</sup> Thus, we confirmed that the additional supplement by the  $\text{Co}^{3+/4+}$  redox pair might be beneficial for enhancing the electrical conductivity of  $\text{Na}_{0.6}[\text{Mg}_{0.2}\text{Mn}_{0.8}]\text{O}_2$ , which promotes facile charge transfer even at high rates. Comparison of the pDOS of  $\text{Na}_{0.5}[\text{Mg}_{0.25}\text{Mn}_{0.5}\text{Co}_{0.25}]\text{O}_2$  and fully desodiated  $\text{Na}_0[\text{Mg}_{0.25}\text{Mn}_{0.5}\text{Co}_{0.25}]\text{O}_2$  (Figure 5) confirms that the electron density of the isolated O 2p orbital in the Mg–O–Na configuration was changed to hole density, which implies that the O 2p orbital of  $\text{Na}_{0.5}[\text{Mg}_{0.25}\text{Mn}_{0.5}\text{Co}_{0.25}]\text{O}_2$  can provide electrons for  $\text{Na}^+$  deintercalation from the structure and that its  $\text{O}^{2-/-1-}$  redox reaction is possible. In addition, first-principles calculations using the nudged elastic band (NEB) method confirmed that

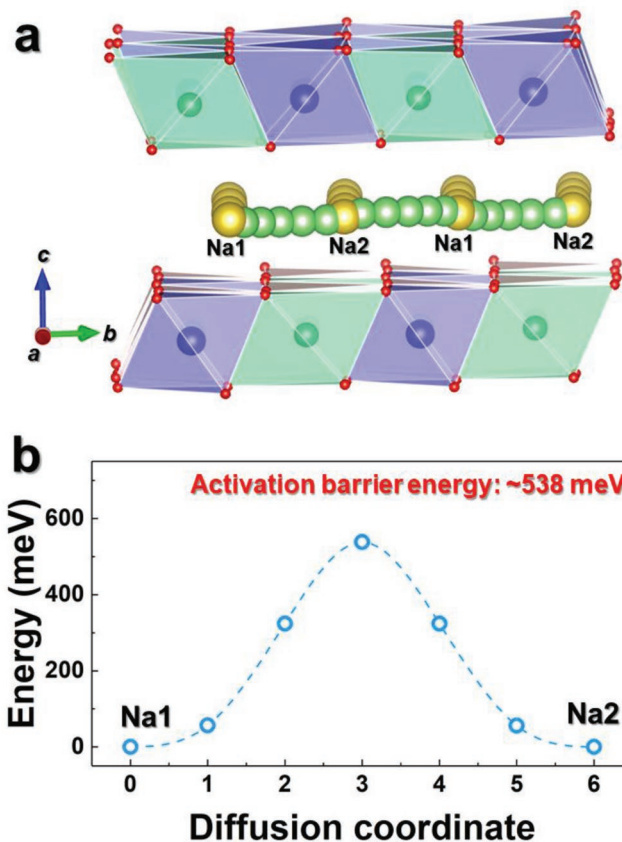


**Figure 6.** a) NEB calculation of activation barrier energy for  $\text{Na}^+$  diffusion in  $\text{Na}_1[\text{Mg}_{0.25}\text{Mn}_{0.5}\text{Co}_{0.25}]\text{O}_2$ . b)  $\text{Na}_1$ – $\text{Na}_2$  diffusion pathways in  $\text{Na}_1[\text{Mg}_{0.25}\text{Mn}_{0.5}\text{Co}_{0.25}]\text{O}_2$ .

an activation energy of  $\approx 538$  meV is required for  $\text{Na}^+$  ionic diffusion in the  $ab$  plane of the  $\text{Na}_1[\text{Mg}_{0.25}\text{Mn}_{0.5}\text{Co}_{0.25}]\text{O}_2$  structure (Figure 6), which is a reasonable value for facial  $\text{Na}^+$  diffusion and is smaller than that for  $\text{Na}_1[\text{Mg}_{0.25}\text{Mn}_{0.75}]\text{O}_2$  (Figure S11, Supporting Information). These predictions based on first-principles calculations imply that Co substitution may enable significant enhancement of not only the electronic conductivity but also the ionic conductivity of  $\text{Na}_x[\text{Mg}_{0.2}\text{Mn}_{0.8}]\text{O}_2$ , resulting in the excellent power capability of  $\text{Na}_x[\text{Mg}_{0.2}\text{Mn}_{0.6}\text{Co}_{0.2}]\text{O}_2$  and demonstrating its potential as a promising cathode material for SIBs.

Ex situ XRD and high-resolution transmission electron microscopy (HR-TEM) measurements were performed on an extensively cycled  $\text{Na}_{0.6}[\text{Mg}_{0.2}\text{Mn}_{0.6}\text{Co}_{0.2}]\text{O}_2$  electrode (Figure S12, Supporting Information). As shown in Figure S12a in the Supporting Information, peak broadening was observed after 1000 cycles. Assuming the  $P6_3/mmc$  space group, after 1000 cycles, the calculated  $a$  lattice parameter increased from 2.8772(1) to 2.9802(1) Å, and the calculated  $c$  lattice parameter decreased from 11.1405(1) to 11.0188(1) Å (Table S2, Supporting Information). However, the crystal structure remained stable, as confirmed by the HR-TEM results in Figure S12b–e in the Supporting Information.

The thermal stability of desodiated  $\text{Na}_{0.16}[\text{Mg}_{0.2}\text{Mn}_{0.8}]\text{O}_2$  and  $\text{Na}_{0.07}[\text{Mg}_{0.2}\text{Mn}_{0.6}\text{Co}_{0.2}]\text{O}_2$  charged to 4.6 V were investigated

using differential scanning calorimetry (DSC) (Figure S13, Supporting Information). These compounds exhibited exceptionally high exothermic onset temperatures (287 °C for  $\text{Na}_{0.16}[\text{Mg}_{0.2}\text{Mn}_{0.8}]\text{O}_2$  and 308 °C for  $\text{Na}_{0.07}[\text{Mg}_{0.2}\text{Mn}_{0.6}\text{Co}_{0.2}]\text{O}_2$ ). Such high exothermic decomposition temperatures may originate from the intrinsic properties of Mn-based compounds, as we have learned from Mn-based cathode materials for LIBs.<sup>[39]</sup> It is worth noting that the exothermic decomposition process was delayed for  $\text{Na}_{0.07}[\text{Mg}_{0.2}\text{Mn}_{0.6}\text{Co}_{0.2}]\text{O}_2$ , although more capacity was delivered for the electrode. In the charged state, these compounds have oxidized oxygen atoms from  $\text{O}^{2-}$  to  $\text{O}^{1-}$  in the crystal structure, such that the exothermic decomposition may cause the abrupt release of the oxidized oxygen from the crystal structure. The generated exothermic heat was higher than that for  $\text{Na}_{2/3}[\text{Ni}_{0.2}\text{Mn}_{0.8}]\text{O}_2$  activated by the  $\text{Ni}^{2+/4+}$  redox pair.<sup>[41]</sup> Further work is necessary to relate the heat generation to the oxygen redox during the exothermic reaction.

### 3. Conclusion

The structural and electrochemical properties of the layered  $\text{Na}_{0.6}[\text{Mg}_{0.2}\text{Mn}_{0.8-x}\text{Co}_x]\text{O}_2$  ( $x = 0.0-0.2$ ) compounds are investigated. The partial substitution of Mn with Co has positive effects on both the structural and electrochemical performance. The higher capacity of  $\text{Na}_{0.6}[\text{Mg}_{0.2}\text{Mn}_{0.6}\text{Co}_{0.2}]\text{O}_2$  is attributed to the overlapping of the Co 3d and O 2p orbitals in the crystal structure. The calculation results indicate that the incorporation of Co leads to a decrease of the bandgap from  $\approx 2.65$  to  $\approx 0.61$  eV, which explains the outstanding performance of  $\text{Na}_{0.6}[\text{Mg}_{0.2}\text{Mn}_{0.6}\text{Co}_{0.2}]\text{O}_2$  assisted by the  $\text{O}^{2-/1-}$  redox pair. Hence, the long-term cycling stability observed at 5C can be understood. To the best of our knowledge, the achieved results represent the best electrochemical performance among oxygen-redox-based materials, particularly for long-term cycling (Table S3, Supporting Information).

### 4. Experimental Section

**Preparation:** The P2-type  $\text{Na}_{0.6}[\text{Mg}_{0.2}\text{Mn}_{0.8-x}\text{Co}_x]\text{O}_2$  ( $x = 0.0-0.2$ ) compounds were synthesized using a spray pyrolysis method.  $\text{NaNO}_3$  (99%, Samchun),  $\text{Mn}(\text{NO}_3)_2 \cdot 4\text{H}_2\text{O}$  ( $\geq 97\%$ , Sigma-Aldrich),  $\text{Mg}(\text{NO}_3)_2 \cdot 6\text{H}_2\text{O}$  ( $\geq 98.0\%$ , Sigma-Aldrich),  $\text{Co}(\text{NO}_3)_2 \cdot 6\text{H}_2\text{O}$  ( $\geq 98.0\%$ , Sigma-Aldrich), citric acid ( $\geq 99.5$ , Junsei), and sucrose ( $\geq 99.5$ , Samchun) were used as starting materials for the spray pyrolysis. Details of the synthetic process are described in the prior work.<sup>[42]</sup> Calcination was conducted at 870 °C in air to obtain the P2-type  $\text{Na}_{0.6}[\text{Mg}_{0.2}\text{Mn}_{0.8-x}\text{Co}_x]\text{O}_2$  ( $x = 0.0-0.2$ ). The compounds were stored in an Ar-filled glove box to minimize the moisture contact during storage.

**Characterization:** Powder X-ray diffraction (PANalytical, Empyrean) using Cu K $\alpha$  radiation was employed to identify the crystalline phases of the as-prepared P2-type  $\text{Na}_{0.6}[\text{Mg}_{0.2}\text{Mn}_{0.8-x}\text{Co}_x]\text{O}_2$  ( $x = 0.0-0.2$ ) powders. Measurements were performed between 10° and 110° (2 $\theta$ ) with a step size of 0.03°. The FullProf Rietveld program was used to refine the crystalline character of the synthesized powders.<sup>[43]</sup> Operando XRD (PANalytical, Empyrean) using Cu K $\alpha$  radiation was also employed to analyze the structural variation in the 2 $\theta$  range between 10° and 50° with a step size of 0.03° during the cycle. The resulting lattice parameters were refined using the CELREF program.<sup>[44]</sup> The produced powders were examined using scanning electron microscopy (SEM; SU-8010,

Hitachi) to analyze morphology of  $\text{Na}_{0.6}[\text{Mg}_{0.2}\text{Mn}_{0.8-x}\text{Co}_x]\text{O}_2$  ( $x = 0.0-0.2$ ) powders. Differential scanning calorimetry (Pyris 1, Perkin-Elmer) measurements were performed at a temperature scan rate of 1 °C min<sup>-1</sup> to analyze the thermal stability of desodiated electrodes.

**Electrochemical Tests:** For electrochemical evaluation, the as-synthesized  $\text{Na}_{0.6}[\text{Mg}_{0.2}\text{Mn}_{0.8-x}\text{Co}_x]\text{O}_2$  ( $x = 0.0-0.2$ ) powders were mixed with Super P and polyvinylidene fluoride (PVDF) binder in a weight ratio of 8:1:1 in *N*-methyl-2-pyrrolidone (NMP). The prepared slurry was cast onto aluminum foil. R2032 coin-type cells using Na metal as the negative electrode were assembled for electrochemical cell tests. The electrolyte solution was 0.5 M NaPF<sub>6</sub> in a mixed solvent of propylene carbonate (PC) and fluoroethylene carbonate (FEC) in a volume ratio of 98:2. The fabricated cells were charged and then discharged between 1.5 and 4.6 V at a rate of 0.1C (26 mA g<sup>-1</sup>), and the current was further raised to 5C (1.3 A g<sup>-1</sup>) for a long-term cycle test at 25 °C.

**Post Cycle Electrode Analysis:** X-ray absorption near edge structure spectroscopy was employed to understand the variation in the oxidation states of the transition metals and oxygen. The analysis was performed at the 7D X-ray absorption fine structure (XAFS) beamline and 4D beamline, respectively, at the Pohang Accelerator Laboratory (PAL), Pohang, South Korea. Transmission electron microscopy (JEM-F200, JEOL) was used to analyze structural factors of the pristine  $\text{Na}_{0.6}[\text{Mg}_{0.2}\text{Mn}_{0.6}\text{Co}_{0.2}]\text{O}_2$  electrode and the electrode after 1000 cycles.

**Computational Details:** Density functional theory calculations were performed using the projector augmented wave method implemented in the Vienna ab initio simulation package (VASP).<sup>[45-47]</sup> Projector-augmented wave (PAW) pseudopotentials<sup>[48]</sup> were used with a plane-wave basis set as implemented in VASP. Perdew-Burke-Ernzerhof (PBE) parameterization of the generalized gradient approximation (GGA)<sup>[49]</sup> was used for the exchange-correlation functional. The *U* values of Mn and Co for the GGA+*U*-based DFT calculations were 3.9 and 4.0 eV, respectively.<sup>[38]</sup> All the calculations were performed with an energy cutoff of 500 eV until the residual forces in the system converged to less than 0.05 eV Å<sup>-1</sup> per unit cell. A 2 × 2 × 1 supercell was applied for these DFT calculations. The cluster-assisted statistical mechanics (CASM) software was used to generate all the Na/vacancy and Mg/Co/Mn configurations for each composition followed by full DFT calculations on a maximum of 30 configurations with the lowest electrostatic energy for each composition to obtain the most optimal crystal structural information for  $\text{Na}_{0.5}[(\text{Mg}^{2+})_{0.25}(\text{Mn}_{0.75-x}\text{Co}_x)]^{4+}_{0.75}]\text{O}_2$ .<sup>[50]</sup> For the DOS calculations, the Heyd-Scuseria-Ernzerhof hybrid functional (HSE06) was used, as it has been found to accurately reproduce the O 2p states for transition metal oxides. Nudged elastic band calculations were performed to determine the activation barrier for Na<sup>+</sup> diffusion in the  $\text{Na}_1[\text{Mg}_{0.25}\text{Mn}_{0.75-x}\text{Co}_x]\text{O}_2$  structures ( $x = 0, 0.25$ ).<sup>[51]</sup> A unit cell created from five formula units of the  $\text{Na}_1[\text{Mg}_{0.25}\text{Mn}_{0.75-x}\text{Co}_x]\text{O}_2$  structures with one generated vacancy was used to model the Na<sup>+</sup> diffusion. Five intermediate states were considered between the first and final images of a single Na<sup>+</sup> diffusion event. During the NEB calculation, all the structures were allowed to relax with fixed lattice parameters.

### Supporting Information

Supporting Information is available from the Wiley Online Library or from the author.

### Acknowledgements

H.J.K. and A.K. contributed equally to this work. This research was supported by the International Research & Development Program of the National Research Foundation of Korea (NRF) funded by the Ministry of Science and ICT of Korea (NRF-2017K1A3A1A30084795, NRF-2015M3D1A1069713, and NRF-2017R1A2A2A05069634).

## Conflict of Interest

The authors declare no conflict of interest.

## Keywords

DFT, Mn-rich, oxygen redox, P2-type layered cathodes, sodium-ion batteries

Received: April 11, 2019

Revised: May 23, 2019

Published online: July 12, 2019

- [1] M. S. Whittingham, *Prog. Solid State Chem.* **1978**, *12*, 41.
- [2] C. Delmas, J. Braconnier, C. Fouassier, P. Hagemuller, *Solid State Ionics* **1981**, *3–4*, 165.
- [3] J. J. Braconnier, C. Delmas, P. Hagemuller, *Mater. Res. Bull.* **1982**, *17*, 993.
- [4] A. Maazaz, C. Delmas, P. Hagemuller, *J. Inclusion Phenom.* **1983**, *1*, 45.
- [5] A. Mendiboure, C. Delmas, P. Hagemuller, *J. Solid State Chem.* **1985**, *57*, 323.
- [6] J.-Y. Hwang, S.-T. Myung, Y.-K. Sun, *Chem. Soc. Rev.* **2017**, *46*, 3529.
- [7] M. H. Han, E. Gonzalo, G. Singh, T. Rojo, *Energy Environ. Sci.* **2015**, *8*, 81.
- [8] N. Ortiz-Vitoriano, N. E. Drewett, E. Gonzalo, T. Rojo, *Energy Environ. Sci.* **2017**, *10*, 1051.
- [9] C. Delmas, C. Fouassier, P. Hagemuller, *Physica B+C* **1980**, *99*, 81.
- [10] E. Talaie, V. Duffort, H. L. Smith, B. Fultz, L. F. Nazar, *Energy Environ. Sci.* **2015**, *8*, 2512.
- [11] R. Berthelot, D. Carlier, C. Delmas, *Nat. Mater.* **2011**, *10*, 74.
- [12] Z.-Y. Li, R. Gao, L. Sun, Z. Hu, X. Liu, *J. Mater. Chem. A* **2015**, *3*, 16272.
- [13] D. Yuan, X. Hu, J. Qian, F. Pei, F. Wu, R. Mao, X. Ai, H. Yang, Y. Cao, *Electrochim. Acta* **2014**, *116*, 300.
- [14] W. K. Pang, S. Kalluri, V. K. Peterson, N. Sharma, J. Kimpton, B. Johannessen, H. K. Liu, S. X. Dou, Z. Guo, *Chem. Mater.* **2015**, *27*, 3150.
- [15] Y. H. Jung, A. S. Christiansen, R. E. Johnsen, P. Norby, D. K. Kim, *Adv. Funct. Mater.* **2015**, *25*, 3227.
- [16] Y. Wen, B. Wang, G. Zeng, K. Nogita, D. Ye, L. Wang, *Chem. - Asian J.* **2015**, *10*, 661.
- [17] K. Park, D. Han, J. Shon, S. G. Doo, S. Lee, *RSC Adv.* **2015**, *5*, 6340.
- [18] D. Buchholz, C. Vaalma, L. G. Chagas, S. Passerini, *J. Power Sources* **2015**, *282*, 581.
- [19] A. Caballero, L. Hernán, J. Morales, L. Sánchez, J. Santos Peña, M. A. G. Aranda, *J. Mater. Chem.* **2002**, *12*, 1142.
- [20] D. Su, C. Wang, H. Ahn, G. Wang, *Chem. - Eur. J.* **2013**, *19*, 10884.
- [21] N. Yabuuchi, M. Kajiyama, J. Iwatate, H. Nishikawa, S. Hitomi, R. Okuyama, R. Usui, Y. Yamada, S. Komaba, *Nat. Mater.* **2012**, *11*, 512.
- [22] X. Wang, M. Tamaru, M. Okubo, A. Yamada, *J. Phys. Chem. C* **2013**, *117*, 15545.
- [23] D. Yuan, W. He, F. Pei, F. Wu, Y. Wu, J. Qian, Y. Cao, X. Ai, H. Yang, *J. Mater. Chem. A* **2013**, *1*, 3895.
- [24] D. Buchholz, A. Moretti, R. Kloepsch, S. Nowak, V. Siozios, M. Winter, S. Passerini, *Chem. Mater.* **2013**, *25*, 142.
- [25] K. Kubota, N. Yabuuchi, H. Yoshida, M. Dahbi, S. Komaba, *MRS Bull.* **2014**, *39*, 416.
- [26] J. Billaud, G. Singh, A. R. Armstrong, E. Gonzalo, V. Roddatis, M. Armand, T. Rojo, P. G. Bruce, *Energy Environ. Sci.* **2014**, *7*, 1387.
- [27] N. Yabuuchi, H. Hara, K. Kubota, J. Paulsen, S. Kumakura, S. Komaba, *J. Mater. Chem. A* **2014**, *2*, 16851.
- [28] X. Xiang, K. Zhang, J. Chen, *Adv. Mater.* **2015**, *27*, 5343.
- [29] S. Hu, A. S. Pillai, G. Liang, W. K. Pang, H. Wang, Q. Li, Z. Guo, *Electrochem. Energy Rev.* **2019**, *2*, 277.
- [30] U. Maitra, R. A. House, J. W. Somerville, N. Tapia-Ruiz, J. G. Lozano, N. Guerrini, R. Hao, K. Luo, L. Jin, M. A. Pérez-Osorio, F. Massel, D. M. Pickup, S. Ramos, X. Lu, D. E. McNally, A. V. Chadwick, F. Giustino, T. Schmitt, L. C. Duda, M. R. Roberts, P. G. Bruce, *Nat. Chem.* **2018**, *10*, 288.
- [31] M. Sathiya, G. Rousse, K. Ramesha, C. P. Laisa, H. Vezin, M. T. Sougrati, M.-L. Doublet, D. Foix, D. Gonbeau, W. Walker, A. S. Prakash, M. Ben Hassine, L. Dupont, J.-M. Tarascon, *Nat. Mater.* **2013**, *12*, 827.
- [32] E. de la Llave, E. Talaie, E. Levi, P. K. Nayak, M. Dixit, P. T. Rao, P. Hartmann, F. Chesneau, D. T. Major, M. Greenstein, D. Aurbach, L. F. Nazar, *Chem. Mater.* **2016**, *28*, 9064.
- [33] X. Rong, J. Liu, E. Hu, Y. Liu, Y. Wang, J. Wu, X. Yu, K. Page, Y.-S. Hu, W. Yang, H. Li, X.-Q. Yang, L. Chen, X. Huang, *Joule* **2018**, *2*, 125.
- [34] Q. Li, Y. Qiao, S. Guo, K. Jiang, Q. Li, J. Wu, H. Zhou, *Joule* **2018**, *2*, 1134.
- [35] J. B. Goodenough, K.-S. Park, *J. Am. Chem. Soc.* **2013**, *135*, 1167.
- [36] Z. Lu, J. R. Dahn, *J. Electrochem. Soc.* **2001**, *148*, A1225.
- [37] A. Konarov, J. H. Jo, J. U. Choi, Z. Bakenov, H. Yashiro, J. Kim, S.-T. Myung, *Nano Energy* **2019**, *59*, 197.
- [38] D.-H. Seo, J. Lee, A. Urban, R. Malik, S. Kang, G. Ceder, *Nat. Chem.* **2016**, *8*, 692.
- [39] C. Julien, A. Mauger, K. Zaghbi, H. Groult, *Inorganics* **2014**, *2*, 132.
- [40] *Advances in Lithium-Ion Batteries* (Eds: W. A. vanSchalkwijk, B. Scrosati), Springer, Boston, MA **2002**, pp. 1–5.
- [41] A. Konarov, J. U. Choi, Z. Bakenov, S.-T. Myung, *J. Mater. Chem. A* **2018**, *6*, 8558.
- [42] J. U. Choi, C. S. Yoon, Q. Zhang, P. Kaghazchi, Y. H. Jung, K.-S. Lee, D.-C. Ahn, Y.-K. Sun, S.-T. Myung, *J. Mater. Chem. A* **2019**, *7*, 202.
- [43] T. Roisnel, J. Rodríguez-Carvajal, *FullProf Manual*, **2002**, p. 139.
- [44] J. Laugier, B. Bochu, *ENSP/Laboratoire des Matériaux et du Génie Physique, BP 46. 38042 Saint Martin d'Hères, France.*
- [45] G. Kresse, D. Joubert, *Phys. Rev. B* **1999**, *59*, 1758.
- [46] G. Kresse, J. Furthmüller, *Comput. Mater. Sci.* **1996**, *6*, 15.
- [47] G. Kresse, J. Furthmüller, *Phys. Rev. B* **1996**, *54*, 11169.
- [48] P. E. Blöchl, *Phys. Rev. B* **1994**, *50*, 17953.
- [49] J. P. Perdew, K. Burke, M. Ernzerhof, *Phys. Rev. Lett.* **1996**, *77*, 3865.
- [50] A. Van der Ven, J. C. Thomas, Q. Xu, J. Bhattacharya, *Math. Comput. Simul.* **2010**, *80*, 1393.
- [51] G. Henkelman, B. P. Uberuaga, H. Jónsson, *J. Chem. Phys.* **2000**, *113*, 9901.